Journal of Materials Science: Materials in Electronics (2020) 31:3146–3158
https://doi.org/10.1007/s10854-020-02861-6

Structural, magnetic, and electrical characterization of Sr-substituted $LaFeO_3$ perovskite synthesized via sucrose auto-combustion route

M. A. Gabal[1,2] · F. Al-Solami[1,3] · Y. M. Al Angari[1] · A. Awad[2] · A. A. Al-Juaid[3] · A. Saeed[4]

Received: 24 November 2019 / Accepted: 3 January 2020 / Published online: 10 January 2020

Abstract
In this work, a series of Sr-substituted lanthanum orthoferrite perovskites, $La_{1-x}Sr_xFeO_3$ ($x=0.0$, 0.2, 0.4, 0.6, 0.8, and 1.0), were prepared using the sucrose-assisted auto-combustion route to study the effect of Sr-substitution on the structural, magnetic, and electrical properties and to investigate the impact of the entire method on different properties. The auto-combustion process and the perovskites formation were followed using differential thermal analysis–thermogravimetry techniques. The obtained different phases were characterized using X-ray diffractometer (XRD), Fourier transform infrared spectroscopy, and high-resolution transmission electron microscopy HRTEM measurements. XRD revealed peaks attributed to $SrCO_3$ secondary phase increases in their intensity by increasing Sr-content till predominate at $x=1.0$. It also showed a transfer from orthorhombic symmetry to rhombohedral one by increasing Sr-content. The obvious contraction in the unit cell parameters by Sr-substitution could be attributed to the $Fe^{3+} \rightarrow Fe^{4+}$ oxidation occurred to balance the total charge on molecule. The obvious increase in the magnetization by increasing Sr could be attributed to the formation of Fe^{4+} ions, strengthening the ferromagnetic component through sharing in the double-exchange interaction, Fe^{4+}–O–Fe^{3+}, as well as the formation of oxygen vacancies that disturb the uncompensated surface spin. Ac-conductivity measurements indicated a change in the entire conduction mechanism from electronic to ionic with improving conductivity by increasing Sr-content. Generally, the utilized sucrose method indicated an improvement in the obtained magnetization accompanied by lowering conductivity than previously reported systems in literature.

1 Introduction

Perovskite-type oxides with general formula ABO_3 have been a currently attractive research topic owing to their variable structural, chemical composition, and magnetoelectric coupling effect. They have several interested applications in many areas including, advanced materials, solid-state chemistry, magnetic storage media, sensors, and catalysis [1, 2]. In their structure, the A-sites are occupied with the cations having larger ionic radius and are coordinated to 12 oxygen atoms while the cations with smaller ionic radius are coordinated to 6 oxygen atoms and are situated in B-sites [2]. Due to their high stability, these cation sites could be highly substitutable resulting in mixed ionic-electronic conductivity [3].

Of these perovskites, lanthanum orthoferrite ($LaFeO_3$) has been intensively investigated due to its wide applications in many advanced technologies such as solid oxide fuel cells [4], gas sensors [5], and photo-catalysis [6]. It has an orthorhombic crystal structure [2] with antiferromagnetic properties attributed to the antiparallel alignment of Fe^{3+} spins along a-axis besides the absence of any magnetic interaction between Fe^{3+} ions and nonmagnetic La^{3+} ions [7].

Many investigations have been carried out to enhance its properties through doping or partial substitution to cause valence alternation or oxygen vacancy [8–14]. To achieve this, the dopant or substituent should have less oxidation state than the crystal cations. In literature [7, 15–23], the most intensively studied substituent was strontium, which is a divalent element with larger ionic radii capable of causing oxidation for Fe^{3+} to Fe^{4+} ions and/or creating oxygen

✉ M. A. Gabal
mgabalabdonada@yahoo.com; mgabal@kau.edu.sa

1 Chemistry Department, Faculty of Science, King Abdulaziz University, Jeddah, Kingdom of Saudi Arabia

2 Chemistry Department, Faculty of Science, Benha University, Benha, Egypt

3 Chemistry Department, Faculty of Science, University of Jeddah, Jeddah, Kingdom of Saudi Arabia

4 Physics Department, Faculty of Science, King Abdulaziz University, Jeddah, Kingdom of Saudi Arabia

vacancies that enhance O^{2-} mobility [17]. This substitution was found to enhance extensive modifications in structural, magnetic, electronic as well as catalytic properties of $LaFeO_3$.

Studies on pure and doped $LaFeO_3$ perovskites revealed that the different properties of such materials are strongly influenced by the synthesis routes. In this context, various technique processes were employed for the preparation including solid-state [9], thermal decomposition [7, 21], hot soap [24], polymerization complex [12] microwave-assisted [25], microemulsion [26], electrospinning [23], hydrothermal [27], and auto-combustion [13–18]. Among these methods, the auto-combustion synthesis is considered as the most attractive one due to its simplicity, time saving, cost effective besides its environmentally benign.

In this work, we propose the synthesis of a series of Sr-substituted lanthanum orthoferrite perovskites, $La_{1-x}Sr_xFeO_3$ ($x = 0.0$, 0.2, 0.4, 0.6, 0.8, and 1.0), using sucrose-assisted auto-combustion process. The structural, magnetic as well as the electrical properties of the system were characterized using XRD, Fourier transform infrared spectroscopy (FT-IR), TEM, VSM, ac-conductivity, and dielectric measurements. The effect of Sr-substitution on the different properties was investigated and discussed.

2 Experimental procedures

High-purity analytical reagents lanthanum nitrate hexahydrate $La(NO_3)_3{\cdot}6H_2O$, strontium nitrate $Sr(NO_3)_2$, and iron nitrate nonahydrate; $Fe(NO_3)_3{\cdot}9H_2O$ all from BDH were used as starting materials. Liquid ammonia (25% solution, Merck) and commercial sucrose $C_{12}H_{22}O_{11}$ were used as received.

$La_{1-x}Sr_xFeO_3$ perovskite-type ferrites ($x = 0.0$, 0.2, 0.4, 0.6, 0.8, and 1.0) were prepared by sucrose-assisted auto-combustion method [28]. The stoichiometric mole ratios of $La(NO_3)_3{\cdot}6H_2O$, $Sr(NO_3)_2$, and $Fe(NO_3)_3{\cdot}9H_2O$ were weighed and dissolved in distilled water. The sucrose aqueous solution (12 g in 100 ml water) was added to the nitrates mixture during constant stirring at 60 °C. The pH was then adjusted to about 7 using liquid ammonia. The viscous brown gel obtained was then digested at about 90 °C till all water contents completely evaporated. At this point, the gel initiated an auto-combustion process with the generation of large amounts of heat and gases till complete ignition. The obtained as-prepared precursors were then collected, grounded, and stored without any further calcination processes.

The crystallinity as well as the phase formation were characterized using X-ray powder diffractometer (Bruker D8 operated at 40 kV, 25 mA using CuKα irradiation source). The crystals morphology was exhibited using a JEOL 2010 TEM operated at 100 kV. Fourier transform infrared spectrum (FT-IR) was recorded using PerkinElmer (Model USA) spectrophotometer in the range 800–300 cm^{-1}. Magnetic hysteresis loops were recorded at room temperature under field varying ± 10 kOe using vibrating sample magnetometer (VSM-9600 M Lakeshore). The electrical measurements were measured using two-probe method and Hioki LCR high tester 3531 up to 723 K and in the frequency range from 100 Hz to 5 MHz.

3 Results and discussion

3.1 DTA-TG behavior of the as-prepared gel precursor

The study of the thermal decomposition behavior of the obtained viscous brown sucrose gel precursor (as-prepared gel precursor), formed prior to the auto-combustion process, will be helpful in elucidating the proper conditions for the complete synthesis of the entire orthoferrites. Figure 1 showed typical differential thermal analysis–thermogravimetry (DTA-TG) curves in air for the as-prepared gel precursor with $x = 0.0$.

The TG thermogram depicts that the decomposition proceeds through two distinct weight loss regions. The first region indicated a very small weight loss in the range 70–135 °C. The accompanied endothermic DTA change attributed this loss to the dehydration of the gel precursor. In the second region, a continuous progressive mass loss at a steady rate was observed up to about 500 °C, accompanied by two successive overlapped exothermic DTA peaks. This main decomposition step could be attributed to the oxidative decomposition of the carbonaceous content of the precursor during the auto-combustion reaction occurring between nitrates (oxidant) and sucrose organic moiety (fuel) [28] with

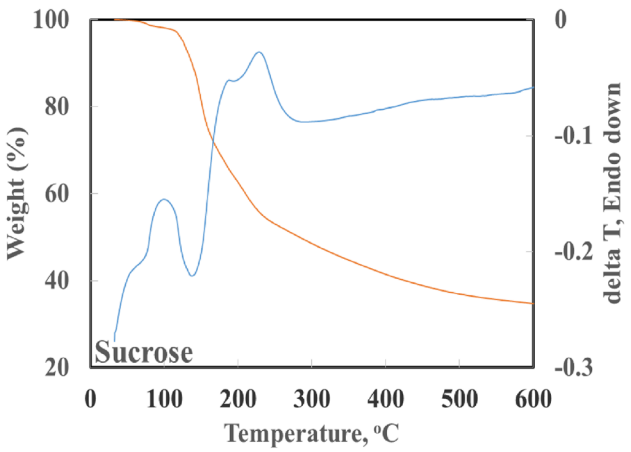

Fig. 1 DTA-TG curves of gel precursor with $x = 0.0$

the formation of stable product phase. The absence of sharp DTA peak around 150 °C attributed to the melting of sucrose [29] suggesting the complete chelation with the entire metal ions. A similar decomposition behavior was obtained for $NiFe_2O_4$ prepared via sucrose auto-combustion route [30].

The absence of any further weight loss or DTA changes suggesting the formation of orthoferrite phase without any indication for the presence of any organic residue. A typical expected combustion reaction between nitrates and sucrose moiety (for precursor with $x = 0.2$) could be represented as

$$0.2Sr(NO_3)_2 + 0.8La(NO_3)_3{\cdot}6H_2O + Fe(NO_3)_3{\cdot}9H_2O + C_{12}H_{22}O_{11} + 4.8O_2 = La_{0.8}Sr_{0.2}FeO_3 + 12CO_2 + 2.9N_2 + 24.8H_2O.$$

3.2 X-ray diffraction characterization

XRD measurements were carried out to identify the crystalline phases formed in $La_{1-x}Sr_xFeO_3$ system ($x = 0.0$–0.1) during sucrose auto-combustion and to study the effect of Sr-substitution on different structural parameters. Figure 2 displayed XRD patterns of the as-prepared precursors up to Sr-content of 0.8. On comparison with the JCPDS card file No. 37-1493 of $LaFeO_3$ perovskite-type, it can be observed that the sample without any Sr-content ($x = 0.0$) exhibited single-phase orthorhombic crystalline $LaFeO_3$ perovskite with reflection planes (101), (121), (220), (202), (141), (240), (143), and (204).

XRD pattern of the sample with Sr-content of $x = 0.2$ showed the same $LaFeO_3$ crystalline phase accompanied by the appearance of very weak diffraction peaks attributed to the formation of $SrCO_3$ secondary phase. The appearance of such impurities could be attributed to the incomplete reaction between the combustion products with the formation of SrO on the surface of $LaFeO_3$ particles, converted into $SrCO_3$ phase by the chemisorption of CO_2 gas from surrounding atmosphere at ambient temperature [31, 32]. The only changes obtained in the diffraction pattern of the sample with Sr-content of 0.4 are the transformation of $LaFeO_3$ crystal form from orthorhombic to rhombohedral symmetry (according to JCPDS card file No. 82-1961 attributed to $La_{0.8}Sr_{0.2}FeO_3$) besides the very slight increase in the intensity of $SrCO_3$ diffraction peaks. Similar transformation behaviors were reported for Sr-substituted $LaFeO_3$ systems [10, 33].

By increasing the Sr-content, it is observed that, both $La_{0.4}Sr_{0.6}FeO_3$ and $La_{0.2}Sr_{0.8}FeO_3$ hold the rhombohedral phase structure with an abrupt increase in the $SrCO_3$ secondary phase diffraction peaks at $x = 0.8$. This result showed that the solubility limit of this system will be up to Sr-content of 0.6 and indicated the inability of solid solution formation after this concentration. XRD pattern of the sample with Sr-content of 1.0 (Fig. 3) showed only the characteristic diffraction peaks attributed to orthorhombic $SrCO_3$ and tetragonal Fe_2O_3 according to the JCPDS cards file No. 84-1778 and 25-1402, respectively. The absence of any diffraction peaks

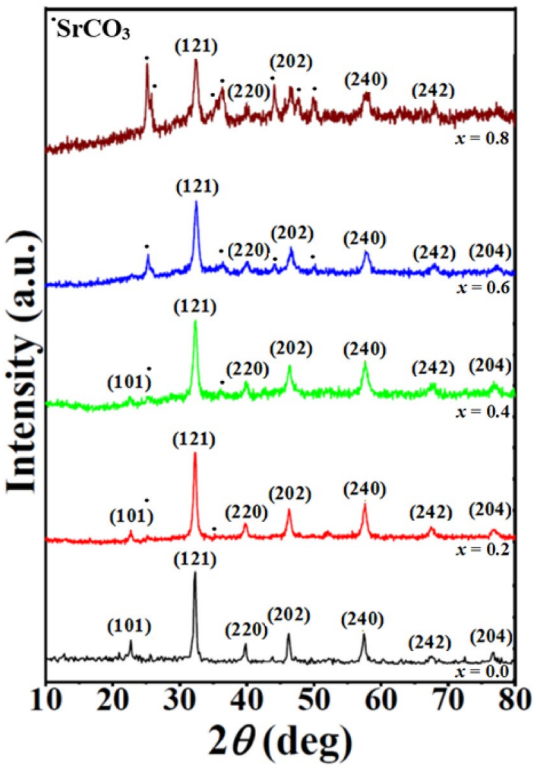

Fig. 2 XRD patterns of $La_{1-x}Sr_xFeO_3$ system ($x = 0.0$–0.8) synthesized via the sucrose method

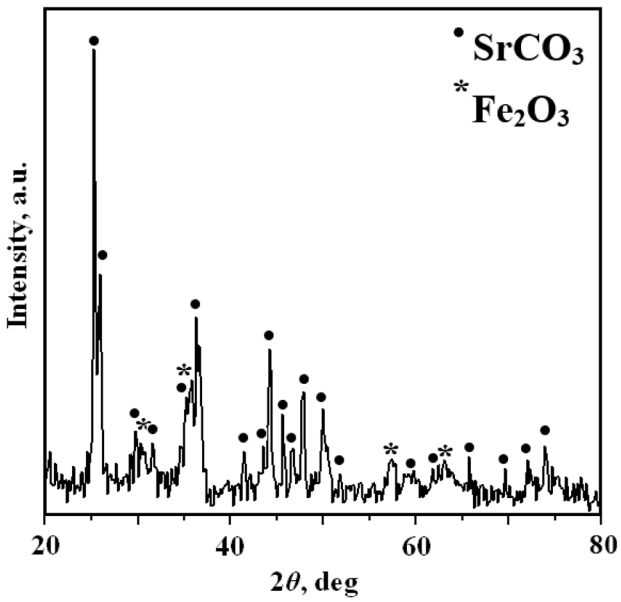

Fig. 3 XRD patterns of the sample with $x = 1.0$

attributed to $SrFeO_3$ revealed the inability of formation at the present experimental conditions.

A closer look at the obtained XRD results and regarding the previous DTA-TG study (Fig. 1) we can conclude that the energy released during the sucrose auto-combustion reaction could be fairly enough for the formation of lanthanum strontium orthoferrites solid solutions up to Sr-content of 0.6 without the needing for any calcination processes, after which further calcination will be required to complete the reaction between the formed oxides and obtain single-phase structure.

The obvious broadening of the obtained diffraction peaks could be attributed to the coexistence of multi-peaks [33] while, their shifts towards higher angles with increasing Sr-content indicated a decrease in the interplanner crystal spacing (*d*-spacing). Similar shifts are observed by other investigators for Sr-doped $LaFeO_3$ [17, 18, 22, 34].

According to the Shannon's tables [35], taking into consideration the ionic radii of the hexacoordinated ions, the ionic radius of Sr^{2+} ions (1.18 Å) is larger than that of La^{3+} ions (1.032 Å) which means an increase in the lattice parameters by increasing Sr-content. Really, the substitution of higher valence state Fe^{3+} ions by lower valence Sr^{2+} ions would result in an oxidation of iron on the B-sites from Fe^{3+} to Fe^{4+} in order to balance the total charge on the molecule [18, 22, 34]. The smaller ionic radius of the formed Fe^{4+} ions (0.585 Å) compared to Fe^{3+} ions (0.645 Å) allowed the entire lattice parameters and thus the unit cell to contract. Overall, this valence change is more dominant than the ionic radius effect and cannot be neglected. In agreement with this contraction in the unit cell parameters, the calculated average crystallite sizes using Scherrer's equation [36], tabulated in Table 1, indicated also a gradual decrease with increasing Sr-content.

3.3 FT-IR analysis

Figure 4 shows the characteristic part of FT-IR spectra for $La_{1-x}Sr_xFeO_3$ nanopowders.

All the spectra showed two broad absorption peaks around 570 and 330 cm^{-1} attributed to M–O contribution [12, 13]. The observed band around 570 cm^{-1} could be assigned to the Fe–O bond stretching vibration while that around 330 cm^{-1} to Fe–O–Fe deformation bending vibration in the octahedral sites. The change in the bands positions as a function of Sr-content is summarized in Table 1. The obvious shift in the bands position values towards higher frequency with successive Sr-substitution confirmed the iron oxidation process previously described. The smaller ionic radius Fe^{4+} ions will shorten and strengthen the Fe–O bond and consequently increasing frequency [21].

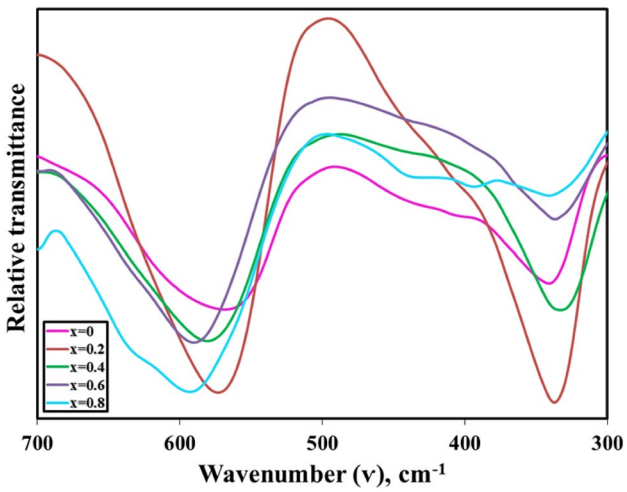

Fig. 4 FT-IR spectra of $La_{1-x}Sr_xFeO_3$ system ($x = 0.0–0.8$)

3.4 TEM images

Figure 5 exhibits TEM and high-resolution transmission electron microscopy (HRTEM) images of the investigated ferrite samples ($x = 0.0–0.8$). From the images a1, b1, c1, d1 and e1 it is obvious that, particulates of agglomerated numerous nanocrystallite particles having irregular shape are appeared. Their estimated average particle sizes showed a gradual decrease with increasing Sr-content in agreement with that obtained from the previous XRD analysis (Table 1). Similar behavior was reported by Lin et al. [37] for Ca-substituted $LaFeO_3$ particles. The clearly resolved lattice fringes obtained from the magnification of a portion of the HRTEM image (Fig. 5e2, a3, b3, c3, d3, and e3) indicated that interplanar spacings agreed well with that

Table 1 Structural and electro-magnetic data for $La_{1-x}Sr_xFeO_3$ system ($x = 0.0–0.8$)

x	Crystal type	L (nm)	D (nm)	ν_1 (cm^{-1})	ν_2 (cm^{-1})	MS (mu/g)	Mr (emu/g)	H_c (Oe)	T_C (K)	σ (ohm^{-1} cm^{-1})
0.0	Orthorhombic	24	22	572	333	0.36	0.040	150	573	1.6×10^{-6}
0.2	Orthorhombic	16	14	570	333	0.45	0.043	365	555	2.7×10^{-8}
0.4	Rhombohedral	15	13	578	335	0.98	0.036	121	533	8.3×10^{-8}
0.6	Rhombohedral	13	12	588	337	2.80	0.165	97	518	7.7×10^{-6}
0.8	Rhombohedral	12	12	590	341	6.84	0.342	85	513	1.8×10^{-5}

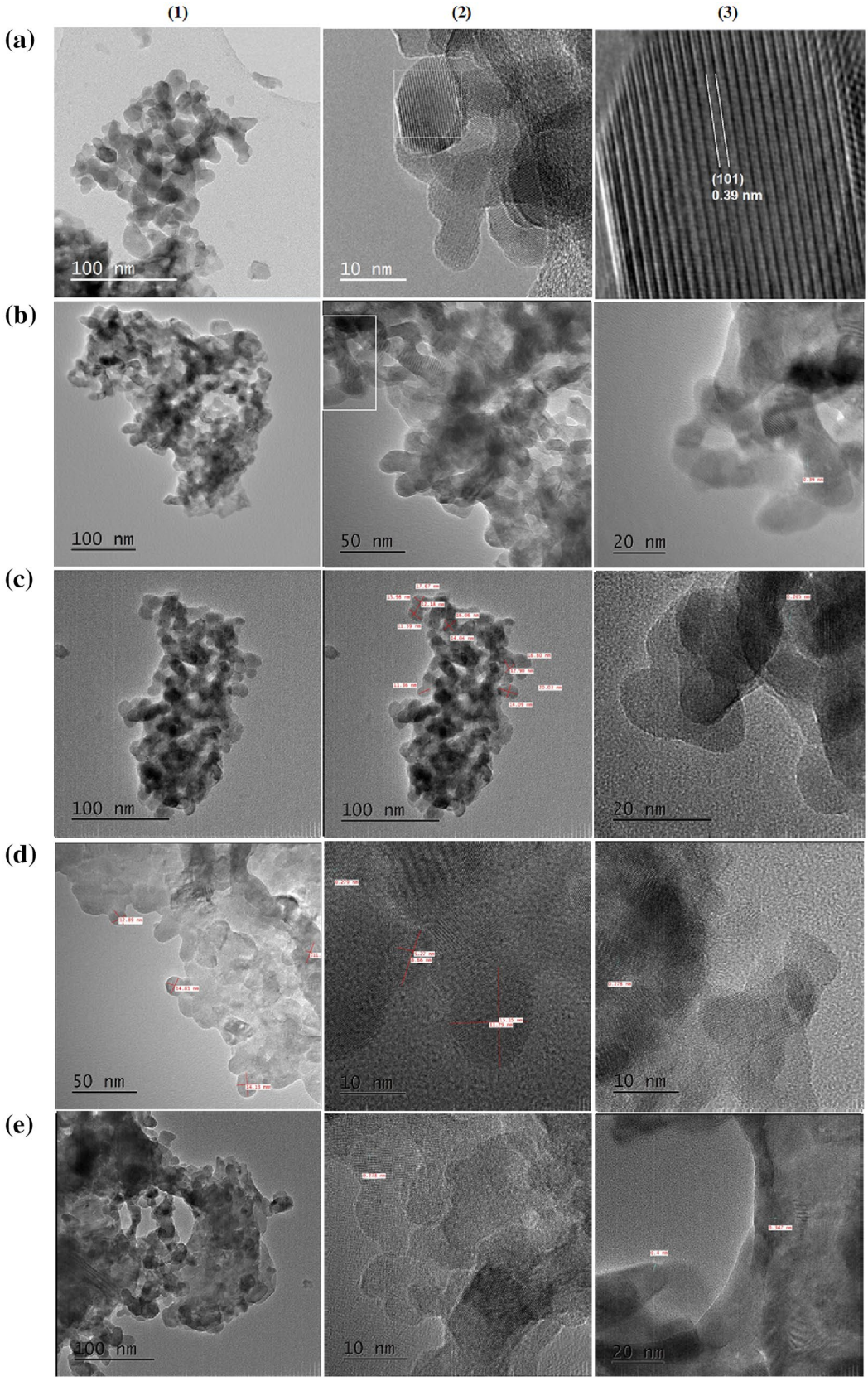

Fig. 5 TEM and HRTEM images of $La_{1-x}Sr_xFeO_3$ system. **a** $x=0.0$, **b** $x=0.2$, **c** $x=0.4$, **d** $x=0.6$, and **e** $x=0.8$

appeared in the XRD patterns. The measured interplanar spacing of 0.39 nm (Fig. 5a3, b3) is consistent with (101) reflection plane of orthorhombic $LaFeO_3$. Also, the observed spacings at 0.265 and 0.278 nm obtained (Fig. 5c3, d3, and e2) are assigned to the reflection plane (121). On the other hand, the appearance of spacings at 0.40 and 0.347 nm (Fig. 5e3) confirmed the presence of $SrCO_3$ secondary phase having diffraction peaks at 2θ angles of 20.3° and 25.9°.

3.5 Magnetic properties

Figure 6 exhibits the magnetization curves at room temperature measured by VSM of $La_{1-x}Sr_xFeO_3$ nanopowders with $x = 0.0$–0.8. As can be seen, the magnetization curves with $x \leq 0.2$ are very narrow, indicating very weak ferromagnetic or antiferromagnetic characterization, while those of the highly doped samples ($x \geq 0.4$) show larger loops characteristic of ferromagnetic behavior. The saturation magnetization (M_s) as well as the remanent magnetization (M_r) values are well enhanced by increasing Sr-content as appeared from Table 1.

The antiferromagnetic behavior of pure $LaFeO_3$ could be attributed to the presence of rare earth La^{3+} ions replacing Fe^{3+} ions and decreasing Fe^{3+}–O–Fe^{3+} interaction [38] or mainly due to the anti-alignment of the two neighboring Fe^{3+} magnetic moments coupled through O^{2-} ions, i.e., super-exchange interaction in antiferromagnetic spin ordering along *a*-axis. However, the very weak ferromagnetically behave of the samples with $x = 0.2$ could be either due to the small crystallite sizes which increases the surface uncompensated spins [12, 39, 40] or the spin canting along the c-axis resulted in tilted of FeO_6 octahedra [7, 23, 41].

Further enhancement in the magnetization by Sr-substitution could be attributed to the formation of Fe^{4+} ions, as

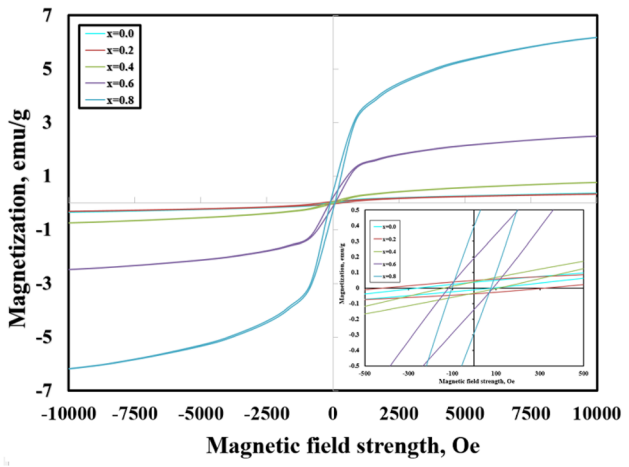

Fig. 6 Room temperature hysteresis loops for $La_{1-x}Sr_xFeO_3$ system ($x = 0.0$–0.8). Inset: Coercivity zoom

previously pointed out in XRD analysis. The formed Fe^{4+} ions resulted in a double-exchange interaction, Fe^{4+}–O–Fe^{3+}, which strengthen the ferromagnetic component. At higher Sr-contents, this double-exchange interaction becomes less significant and the oxygen vacancies resulting from the substitution of higher valence state La^{3+} ions by lower valence Sr^{2+} become more significant. This oxygen vacancies can disturb the uncompensated surface spin and consequently, super-exchange interaction resulting in increasing magnetization [42]. Similar behaviors were obtained for other Sr-substituted systems prepared via different methods [7, 42]. Generally, the present system showed higher magnetization values than those reported by Nforna et al. [7] and Yang [41] for Sr-substituted $LaFeO_3$ prepared via thermal decomposition of mixed metal acetylacetonates and citrate sol–gel method, respectively.

The coercivity values reported in Table 1 showed an abrupt increase by increasing Sr-content to 0.2 followed by a gradual decrease with increasing Sr-content. This large increase could be attributed to the interaction occurred between ferromagnetic Fe^{4+}–O–Fe^{3+} and antiferromagnetic Fe^{4+}–O–Fe^{3+} exchange interactions [43]. The following gradual decrease with increasing Sr-content could be attributed to the decrease in the magneto-crystalline anisotropy. In addition, the coercivity is well known as a microstructure property [44, 45], showed a proportional relation with defects, surface effect, strains, particle size, etc. Thus, regarding Table 1, one can be concluded that the coercivity showed a particle size-dependent behavior since it exhibits a gradual decrease in its value with increasing Sr-content.

4 Electrical properties measurements

4.1 AC-conductivity

Figure 7 illustrates the behavior of ac-conductivity vs. reciprocal temperature for different Sr-substituted samples. The plots followed the Arrhenius relation [28], in which conductivity showing a gradual increase with increasing temperature, except in the temperature range 363–444 K which indicated a gradual decrease with increasing temperature. This decrease is considered as a common behavior of most ferrite [28, 46] in which the successive evaporation of the surface adsorbed water (acting as an electron donor [47]) resulted in decreasing conductivity. Generally, the increase in the conductivity with increasing temperature indicated semiconducting properties of the entire compositions.

It is well known that [17, 34] the Sr^{2+} substitution for La^{3+} ions in $LaFeO_3$ increases its electrical conductivity either by oxidizing Fe^{3+} to Fe^{4+} or increasing O^{2-} mobility through generating oxygen vacancies. In this category, three types of conductivities could arise [34]: The first is

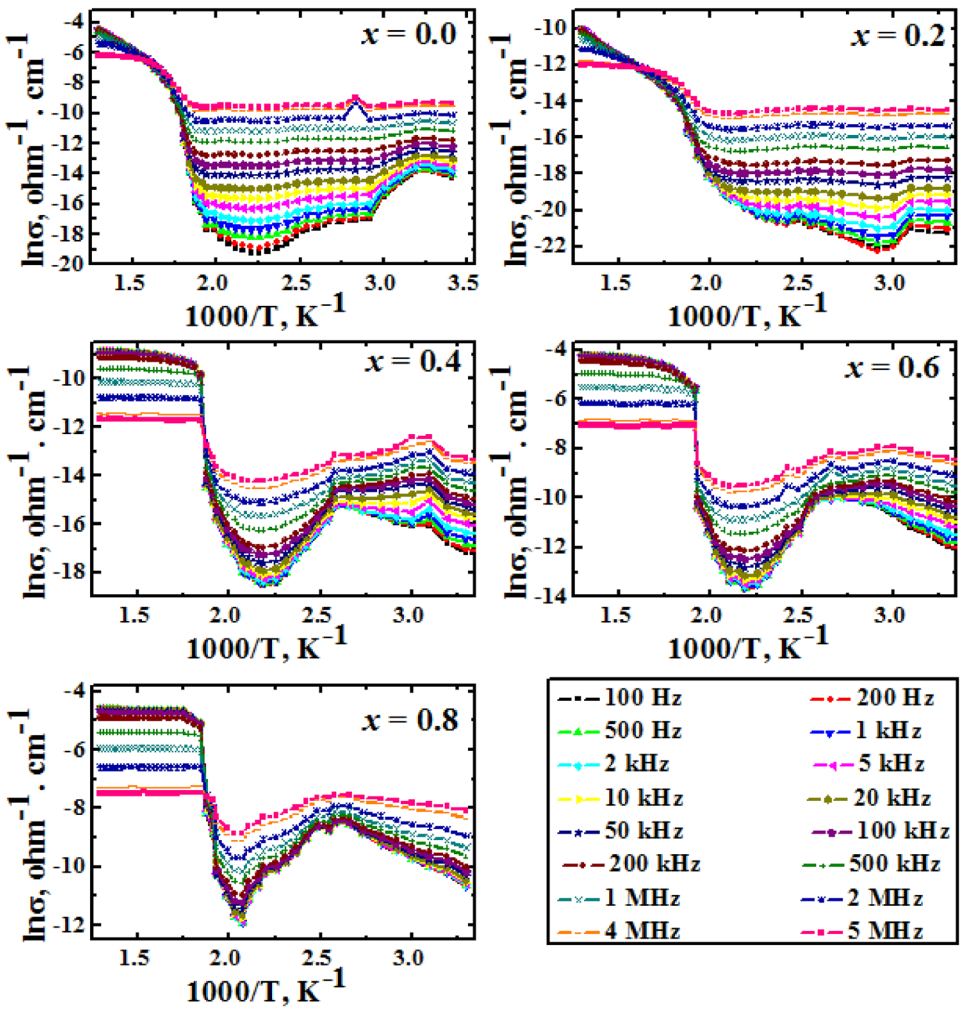

Fig. 7 Relationship between lnσ and the reciprocal of the absolute temperature as a function of the applied frequency for $La_{1-x}Sr_xFeO_3$ system ($x=0.0$–0.8)

the electronic conductivity appeared as a result of increasing charge carriers due to the oxidation of Fe^{3+} to Fe^{4+}, i.e., due to electronic compensation (formula 1); the second is the ionic conductivity attributed to the moving of O^{2-} anion generated from oxygen vacancy, i.e., ionic compensation (formula 2) while the third is a mix of these two previous types (formula 3).

$$\left(La^{3+}_{1-x}Sr^{2+}_{x}\right)\left(Fe^{3+}_{1-x}Fe^{4+}_{x}\right)O_3 \tag{1}$$

$$\left(La^{3+}_{1-x}Sr^{2+}_{x}\right)Fe^{3+}\left(O^{2-}_{3-(x/2)}\delta_{(x/2)}\right) \tag{2}$$

$$\left(La^{3+}_{1-x}Sr^{2+}_{x}\right)\left(Fe^{3+}_{1-y}Fe^{4+}_{y}\right)\left(O^{2-}_{3-((x-y)/2)}\delta_{((x-y)/2)}\right) \tag{3}$$

Thus, the electronic conduction will result in an increase in the average valence of the transition metal cations, while the ionic one reduces oxygen stoichiometry.

The obvious change in the slope of the Arrhenius plot, in the ascending range of conductivity vs. $1/T$, could be attributed to the change in the conduction mechanism. In the first ascending region (low temperature region), the obvious gradual increase in the conductivity with increasing temperature could be assigned to the electronic conduction arised from electron hopping between Fe^{3+} and Fe^{4+} ions. The observed sharp increase in the conductivity at high temperature region indicated the significance of the ionic compensation due to oxygen nonstoichiometry [48].

The ionic conduction predominates only for the higher substituted samples ($x \geq 0.4$) , and the transition temperature (T_C) from electronic to ionic (Table 1) was accompanied by an obvious shift towards lower temperature by increasing Sr-content (Fig. 7), confirming the predominance of the ionic compensation by increasing substitution that disturbing the conductivity. This behavior could be attributed to the changing in the crystal structure from orthorhombic to rhombohedral as reported by Kafa et al. [34].

In addition, due to generating of more charge carriers, the conductivity values obtained at 500 k and 100 kHz for all the investigated samples (Table 1) indicated a gradual increase with increasing Sr-content. The obtained values

are lower than those obtained by Triyono et al. [34] which could be attributed to the difference in the preparation methods. Finally, at higher temperatures, the conductivity of the investigated samples showed a metallic behavior in which conductivity hardly changed with temperature.

4.2 Dielectric properties

Figures 8 and 9 show the dependence of real (ε) and imaginary (ε'') parts of dielectric constant on applied frequency as a function of temperature. The dielectric constants showed a gradual decrease with increasing frequency. A similar dielectric behavior was reported for Sr-substituted $LaFeO_3$ [22, 49]. This decreasing behavior could be attributed to the inability of electrical dipoles to follow the increase in the alternating electrical field [50]. Moreover, the temperature dependence of the dielectric values at lower frequency and temperature independence at higher ones could be assigned to the charge carriers dispersion [51]. This normal behavior of most heterogeneous materials can be explained on the basis of Maxwell and Wagner two-layer model with Koop's phenomenological theory pertaining to space charge polarization due to the hopping $Fe^{+3} \leftrightarrow Fe^{+4}$ at the grain boundaries [52, 53]. Generally, the obtained values of the dielectric constant in this work are lower than that reported by Triyono et al. [22] and

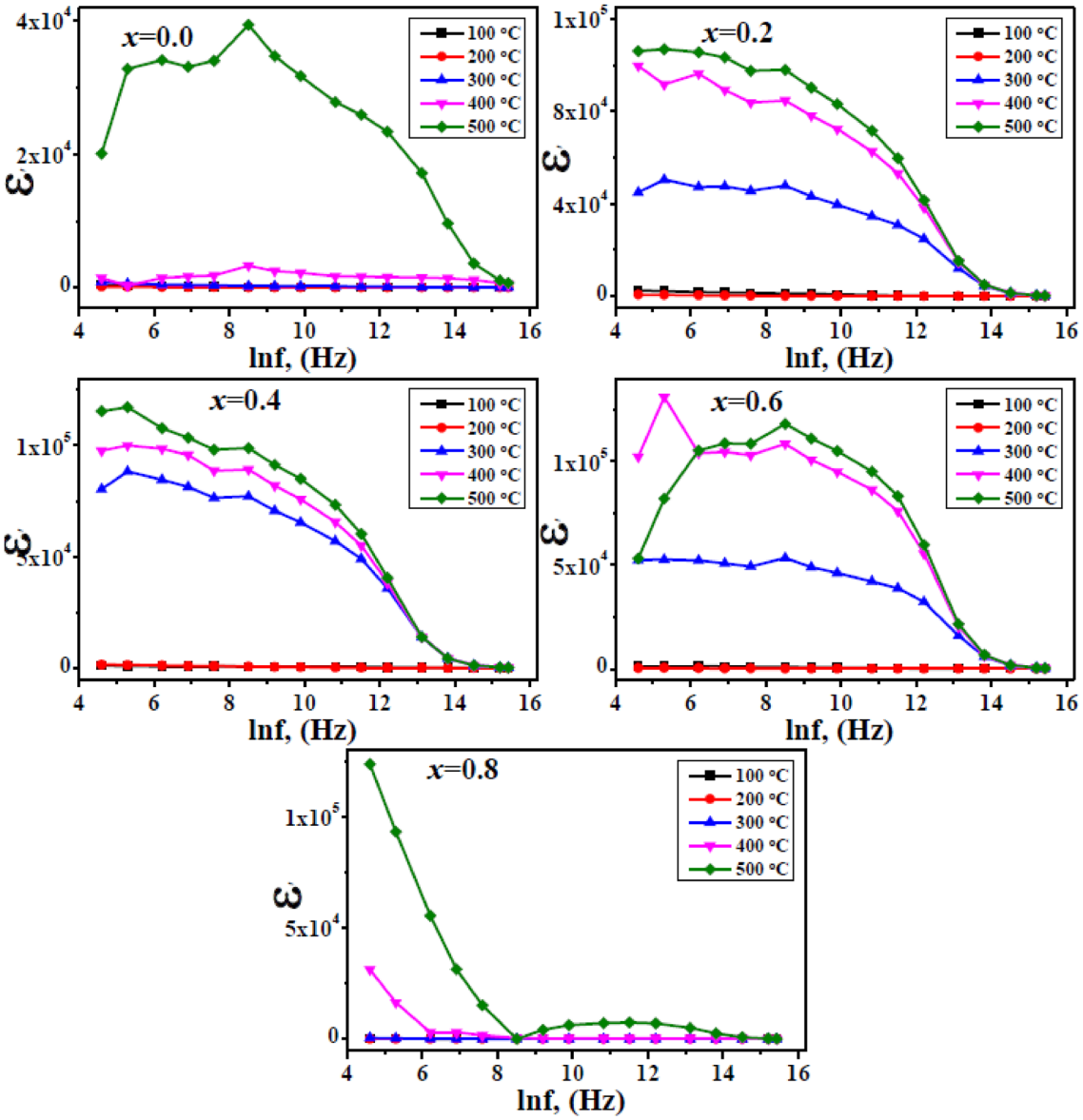

Fig. 8 Relationship between the real part of the dielectric constant (ε) and the frequency as a function of the absolute temperature for $La_{1-x}Sr_xFeO_3$ system ($x = 0.0$–0.8)

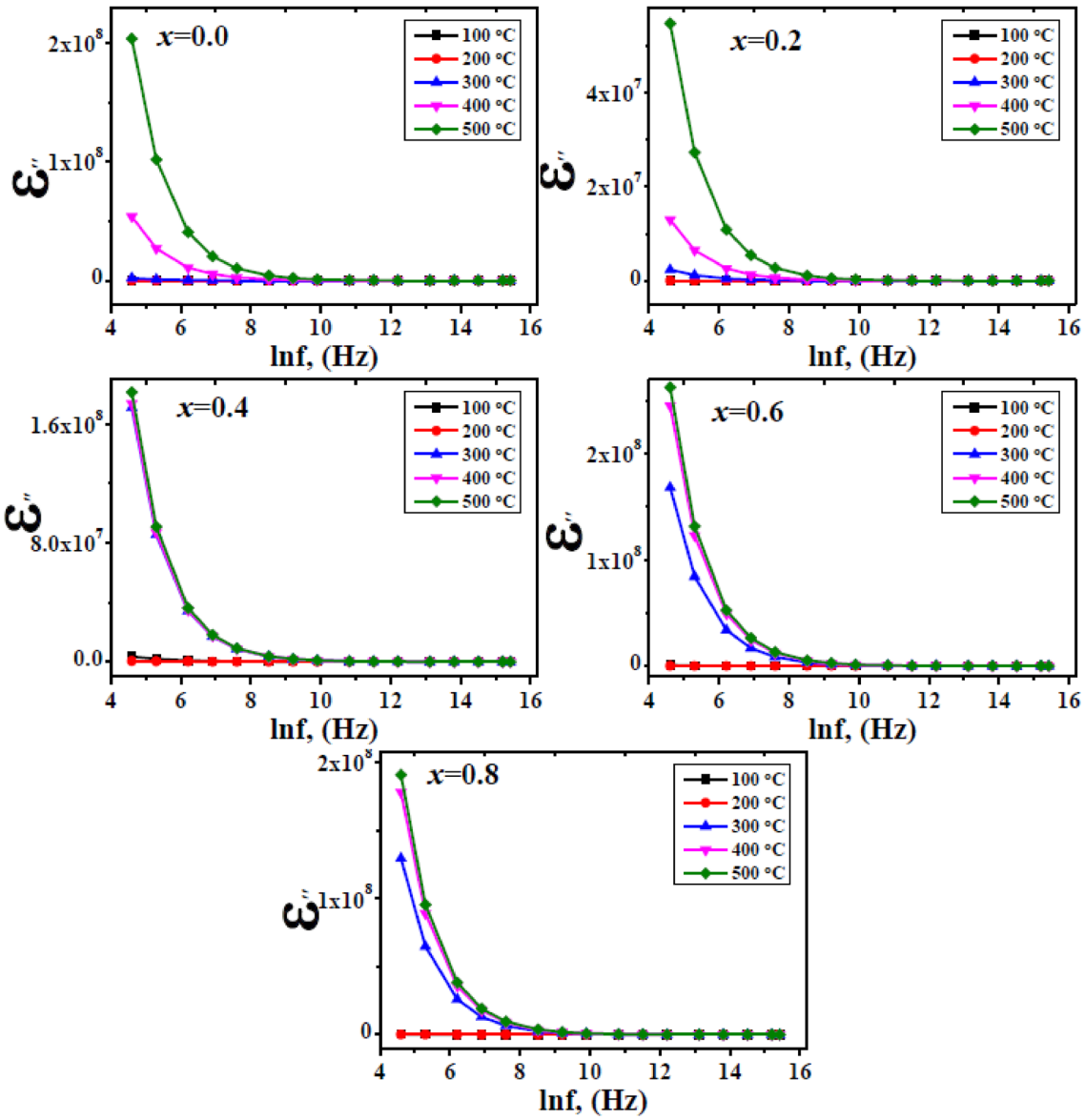

Fig. 9 Relationship between the imaginary part of dielectric constant (ε'') and the frequency as a function of the absolute temperature for $La_{1-x}Sr_xFeO_3$ system ($x = 0.0$–0.8)

Kafa et al. [34] for $La_{1-x}Sr_xFeO_3$ perovskites prepared via citrate sol–gel method.

The nearly constant dielectric behavior at low temperatures changes to a gradual increase at higher ones (Figs. 10 and 11) indicating the ability of the pumping force of temperature in liberating the trapped charge carriers and facilitating dipole orientations, increasing the orientational polarization. The temperature at which the dielectrics started to increase agreed well with that estimated through conductivity measurements (T_C) and could be assigned again to the change in the conduction mechanism.

5 Conclusions

Sr-substituted lanthanum orthoferrite perovskites, $La_{1-x}Sr_xFeO_3$ ($x = 0.0$, 0.2, 0.4, 0.6, 0.8, and 1.0), were prepared using sucrose-assisted auto-combustion process. XRD revealed the appearance of some diffraction peaks attributed to $SrCO_3$ secondary phase with increasing in their intensity by increasing Sr-substitution. The samples with Sr-content ≤ 0.2 indicated orthorhombic phases while those up to Sr-content of 0.8 showed rhombohedral

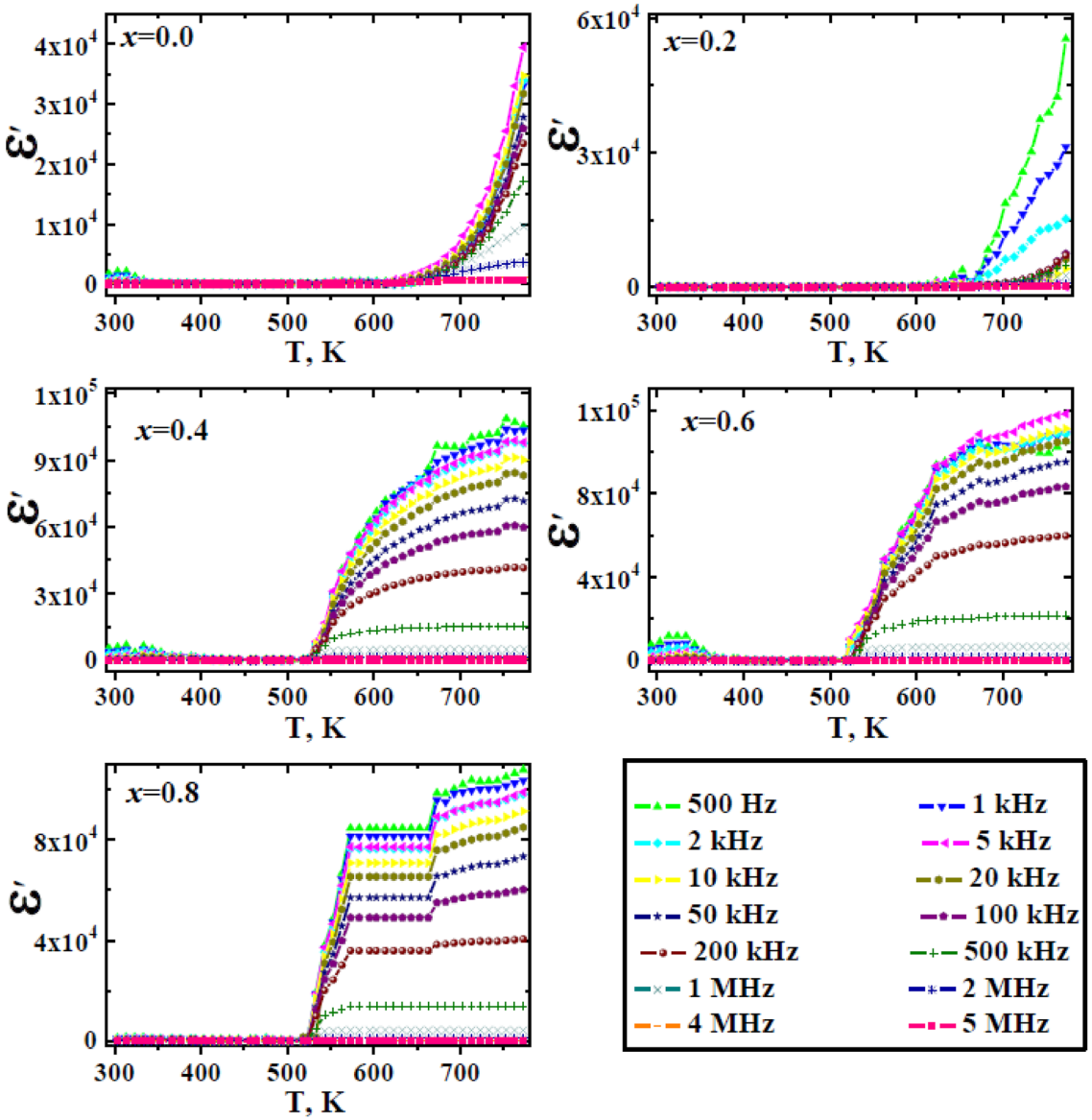

Fig. 10 Relationship between the real part of the dielectric constant (ε) and the absolute temperature as a function of the applied frequency for $La_{1-x}Sr_xFeO_3$ system ($x = 0.0$–0.8)

phase. The obvious shifts in the peaks position towards higher angles, with increasing Sr-content, indicating unit cell contraction arise due to the oxidation of iron from Fe^{3+} to Fe^{4+}. FT-IR spectra confirmed the ferrite formation through two broad absorption peaks around 570 and 330 cm^{-1} attributed to M–O contribution. The Sr-substitution was found to improve the magnetization as well as the conductivity due to the double-exchange interaction, Fe^{4+}–O–Fe^{3+}, and oxygen vacancies formation.

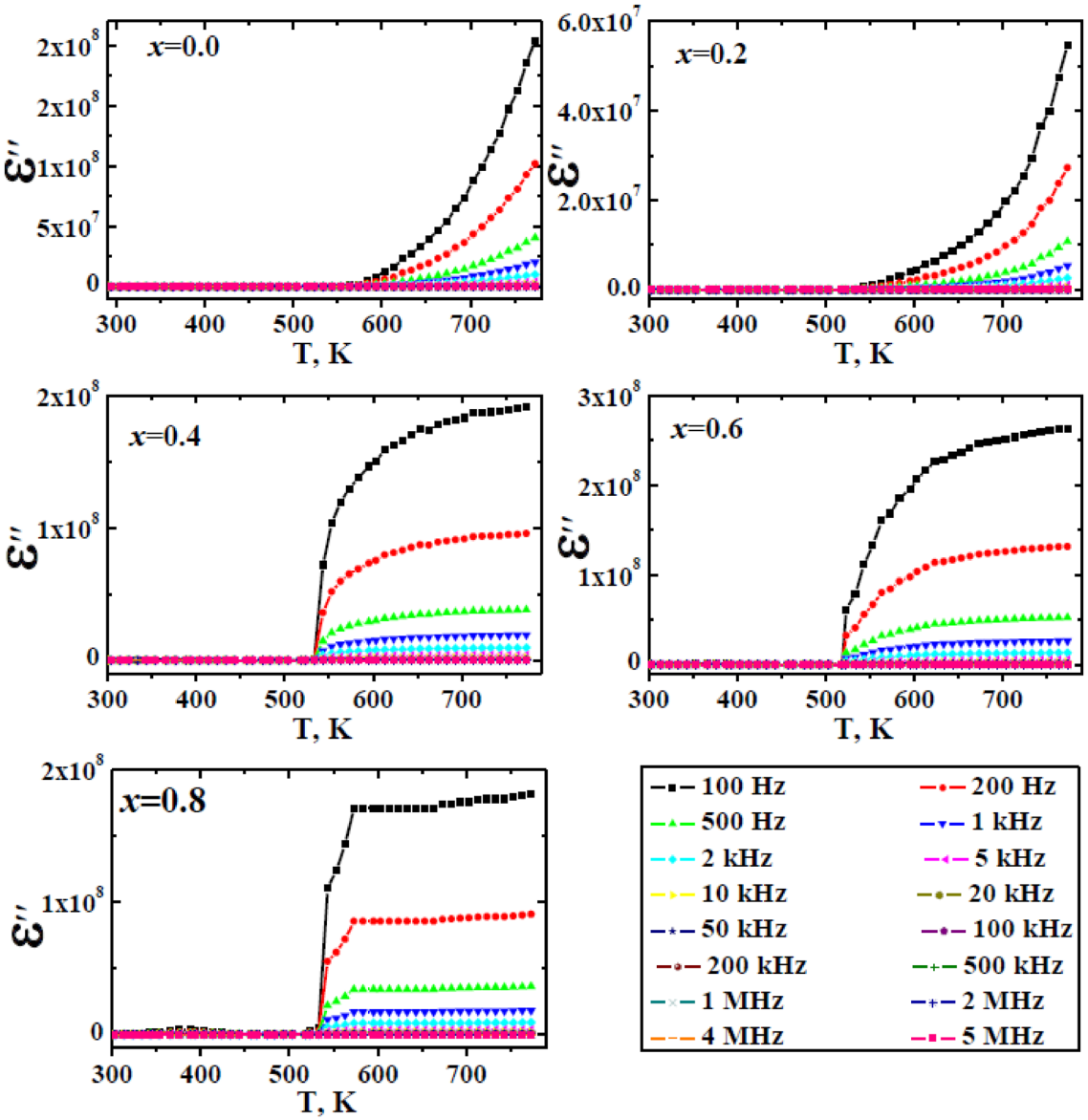

Fig. 11 Relationship between the imaginary part of dielectric constant (ε'') and the absolute temperature as a function of the applied frequency for $La_{1-x}Sr_xFeO_3$ system ($x = 0.0$–0.8)

References

1. J.P. Lin, Z. Guo, M. Li, Q. Lin, K. Huang, Y. He, J. Appl. Biomater. Funct. Mater. **16**, 93 (2018)
2. N. Ramadass, ABO_3-type-oxides-their structure and properties: a bird's eye view. Mater. Sci. Eng. **36**, 231–239 (1978)
3. K. Fan, H. Qin, L. Wang, L. Ju, J. Hu, CO_2 Gas sensors based on $La_{1-x}Sr_xFeO_3$ nanocrystalline powders. Sens. Actuators B **177**, 265–269 (2013)
4. M. Noroozifar, M. Khorasani-Motlagh, M. Ekrami-Kakhki, Enhanced electrocatalytic properties of Pt–Chitosan nanocomposite for direct methanol fuel cell by $LaFeO_3$ and carbon nanotube. J. Power. Sources. **248**, 130–139 (2014)
5. Y.M. Zhang, J. Zhang, J.L. Chen, Z.Q. Zhu, Q.J. Liu, Improvement of response to formaldehyde at Ag-$LaFeO_3$ based gas sensors through incorporation of SWCNTs. Sens. Actuators B **195**, 509–514 (2014)
6. S. Acharya, D.K. Padhi, K.M. Parida, Visible light driven $LaFeO_3$ nano sphere/RGO compositephotocatalysts for efficient water decomposition reactions. Catal. Today. (2017). https://doi.org/10.1016/j.cattod.2017.01.001
7. E.A. Nforna, J.N. Ghogomu, P.A. Joy, J.N. Lambi, Structure and magnetic properties of lanthanum strontium ferrites nanopowders synthesized by thermal decomposition of mixed metal acetyl acetonates. Int. J. Eng. Res. Technol. **4**, 907–914 (2015)
8. J.P. Lin, Z.P. Guo, Q. Lin, Y.L. Wang, K.L. Huang, Y. He, Mater. Sci. **25**, 135 (2019)
9. M. Hung, M.V.M. Rao, D. Tsai, Microstructures and electrical properties of calcium substituted $LaFeO_3$ as SOFC cathode. Mater. Chem. Phys. **101**, 297–302 (2007)

10. X. Dai, C. Yu, Q. Wu, Comparison of $LaFeO_3$, $La_{0.8}Sr_{0.2}FeO_3$, and $La_{0.8}Sr_{0.2}Fe_{0.9}Co_{0.1}O_3$ perovskite oxides as oxygen carrier for partial oxidation of methane. J. Nat. Gas Chem. **17**, 415–418 (2008)
11. K. Mukhopadhyay, A.S. Mahapatra, P.K. Chakrabarti, Multiferroic behavior, enhanced magnetization and exchange bias effect of Zn substituted nanocrystalline $LaFeO_3$ ($La_{(1-x)}Zn_xFeO_3$, x = 010, and 030). J. Magn. Magn. Mater. **329**, 133–141 (2013)
12. Y. Janbutrach, S. Hunpratub, E. Swatsitang, Ferromagnetism and optical properties of $La_{1-x}Al_xFeO_3$ nanopowders nanoscale. Res. Lett. **9**, 498–954 (2014)
13. A. Rai, A.K. Thakur, Effect of co-substitution on structural, optical, dielectric and magnetic behavior of $LaFeO_3$. J. Alloys Compd. **695**, 3579–3588 (2017)
14. Q. Lin, J. Lin, X. Yang, Y. He, L. Wang, J. Dong, The effects of Mg^{2+} and Ba^{2+} dopants on the microstructure and magnetic properties of doubly-doped $LaFeO_3$ perovskite catalytic nanocrystals. Ceram. Int. **45**, 3333–3340 (2019)
15. P.A. Murade, V.S. Sangawar, G.N. Chaudhari, V.D. Kapse, A.U. Bajpeyee, Acetone gas-sensing performance of Sr-doped nanostructured $LaFeO_3$ semiconductor prepared by citrate sol-gel route. Curr. Appl. Phys. **11**, 451–456 (2011)
16. Z. Xiaojing, L. Huaju, L. Yong, S. Wenjie, Structural properties and catalytic activity of Sr-substituted $LaFeO_3$ perovskite. Chin. J. Catal. **33**, 1109–1114 (2012)
17. F. He, X. Li, K. Zhao, Z. Huang, G. Wei, H. Li, The use of $La_{1-x}Sr_xFeO_3$ perovskite-type oxides as oxygen carriers in chemical-looping reforming of methane. Fuel **108**, 465–473 (2013)
18. K. Zhao, F. He, Z. Huang, A. Zheng, H. Li, Z. Zhao, $La_{1-x}Sr_xFeO_3$ perovskites as oxygen carriers for the partial oxidation of methane to syngas. Chin. J. Catal. **35**, 1196–1205 (2014)
19. A. Cyza, A. Kopia, L. Cieniek, J. Kusinski, Structural characterization of Sr doped $LaFeO_3$ thin films prepared by pulsed electron deposition method. Mater. Today **3**, 2707–2712 (2016)
20. A. Cyza, L. Cieniek, A. Kopia, Perovskite $La_{1-x}Sr_xFeO_3$ thin film deposited by laser ablation process. Arch. Metall. Mater. **61**, 1063–1067 (2016)
21. N. Koonsaeng, T. Thaweechai, A. Wisitsoraat, W. Wattanathana, S. Wannapaiboon, S. Chotiwan, C. Veranitisagul, A. Laobuthee, Preparation of Sr-doped $LaFeO_3$ by thermal decomposition of metal organic complex and their gas-sensing properties. SOJ Mater. Sci. Eng. **6**, 1–9 (2018)
22. D. Triyono, C.A. Kafa, H. Laysandra, Effect of Sr-substitution on the structural and dielectric properties of $LaFeO_3$ perovskite materials. J. Adv. Dielect. **5**, 1850063 (2018)
23. W. Wang, B. Lin, H. Zhang, Y. Sun, X. Zhang, H. Yang, Synthesis, morphology and electrochemical performances of perovskite-type oxide $La_xSr_{1-x}FeO_3$ nanofibers prepared by electrospinning. J. Phys. Chem. Sol. **124**, 144–150 (2019)
24. T. Fujii, I. Matsusue, D. Nakatsuka, M. Nakanishi, J. Takada, Synthesis and anomalous magnetic properties of $LaFeO_3$ nanoparticles by hot soap method. Mater. Chem. Phys. **129**, 805–809 (2011)
25. P. Tang, Y. Tong, H. Chen, F. Cao, G. Pan, Microwave-assisted synthesis of nanoparticulate perovskite $LaFeO_3$ as a high active visible-light photocatalyst. Curr. Appl. Phys. **13**, 340–343 (2013)
26. W. Haron, T. Thaweechai, W. Wattanathana, A. Laobuthee, H. Manaspiya, C. Veranitisagul, N. Koonsaeng, Structural characteristics and dielectric properties of $La_{1-x}Co_xFeO_3$ and $LaFe_{1-x}Co_xO_3$ synthesized via metal organic complexes. Energy Proc. **34**, 791–800 (2013)
27. K. Ji, H. Dai, J. Deng, L. Song, S. Xie, W. Han, Glucose-assisted hydrothermal preparation and catalytic performance of porous $LaFeO_3$ for toluene combustion. J. Sol. State Chem. **199**, 164–170 (2013)
28. M.A. Gabal, A.A. Al-Juaid, S.M. Al-Rashed, M.A. Hussein, F. Al-Marzouki, Synthesis, characterization and electromagnetic properties of Zn-substituted $CoFe_2O_4$ via sucrose assisted combustion route. J. Magn. Magn. Mater. **426**, 670–679 (2017)
29. S.T. Beckettb, M.G. Francesconi, P.M. Geary, G. Mackenzie, A.P.E. Maulny, DSC study of sucrose melting. Carbohydr. Res. **341**, 2591–2599 (2006)
30. M.A. Gabal, S. Kosa, T.S. El Muttairi, Magnetic dilution effect of nano-crystalline $NiFe_2O_4$ synthesized via sucrose-assisted combustion route. Ceram. Int. **40**, 675–681 (2014)
31. R. Abazari, S. Sanati, L.A. Saghatforoush, A unique and facile preparation of lanthanum ferrite nanoparticles in emulsion nanoreactors: morphology, structure, and efficient photocatalysis. Mater. Sci. Semicond. Process. **25**, 301–306 (2014)
32. P.V. Gosavi, R.B. Biniwale, Pure phase $LaFeO_3$ perovskite with improved surface area synthesized using different routes and its characterization. Mater. Chem. Phys. **119**, 324–329 (2010)
33. G. Deng, Y. Chen, M. Tao, C. Wu, X. Shen, H. Yang, Electrochemical properties of $La_{1-x}Sr_xFeO_3$ (x = 0.2, 0.4) as negative electrode of Ni–MH batteries. Electrochim. Acta **54**, 3910–3914 (2009)
34. C.A. Kafa, D. Triyono, H. Laysandra, Effect of Sr substitution on the room temperature electrical properties of $La_{1-x}Sr_xFeO_3$ nano-crystalline materials. AIP Conf. Proc. **1862**, 030042 (2017). https://doi.org/10.1063/1.4991146
35. R.D. Shannon, Revised effective ionic radii and systematic studies of interatomic distances in halides and chalcogenides. Acta Crystallogr. Sect. A **32**, 751–767 (1976)
36. M.A. Gabal, R.M. El-Shishtawy, Y.M. Al-Angari, Structural and magnetic properties of nano-crystalline Ni–Zn ferrites synthesized using egg-white precursor. J. Magn. Magn. Mater. **324**, 2258–2264 (2012)
37. Q. Lin, J. Xu, F. Yang, X. Yang, Y. He, The influence of Ca substitution on $LaFeO_3$ nanoparticles in terms of structural and magnetic properties. J. Appl. Biomater. Funct. Mater. **16**, 17–25 (2018)
38. Y. He, C. Lei, Q. Lin, J. Dong, Y. Yu, L. Wang, Mössbauer and structural properties of La-substituted $Ni_{0.4}Cu_{0.2}Zn_{0.4}Fe_2O_4$ nanocrystalline ferrite. Sci. Adv. Mater. **7**, 1809–1815 (2015)
39. R.H. Kodama, S.A. Makhlouf, A.E. Berkowitz, Finite size effects in antiferromagnetic NiO nanoparticles. Phys. Rev. Lett. **79**, 1393–1396 (1997)
40. E. Winkler, R.D. Zyster, M.V. Mansilla, D. Fiorant, Surface anisotropy effects in NiO nanoparticles. Phys. Rev. B **72**, 132409 (2005)
41. F. Yang, X.X. Yang, Q. Lin, R.J. Wang, H. Yang, Y. He, Microstructure and magnetic studies of $La_{1-x}Sr_xFeO_3$ nano particles fabricated by the citrate sol–gel method. Mater. Sci. **25**, 231–237 (2019)
42. J. Li, X. Kou, Y. Qin, H. He, Microstructure and magnetic properties of $La_{1-x}Sr_xFeO_{3-\delta}$ nanoparticles. Phys. State Sol. **191**, 255–259 (2002)
43. E.K. Abdel-Khalek, H.M. Mohamed, Synthesis, structural and magnetic properties of $La_{1-x}Ca_xFeO_3$ prepared by the co-precipitation method. Hyperfine Interact. **222**, 57–67 (2013)
44. P. Mathur, A. Thakur, M. Singh, Effect of nanoparticles on the magnetic properties of Mn–Zn soft ferrite. J. Magn. Magn. Mater **320**, 1364–1369 (2008)
45. Q. Li, W. Wang, Fabrication and properties of $Mn_{0.5}Zn_{0.5}Fe_2O_4$ nanofibers. Solid State Sci. **12**, 1303–1306 (2010)
46. M.A. Gabal, F. Al-Solami, Y.M. Al-Angari, A.A. Al-Juaid, A.A. Ali, K. Huang, M. Alsabban, Auto-combustion synthesis and characterization of perovskite-type $LaFeO_3$ nanocrystals prepared via different routes. Ceram. Int. https://doi.org/10.1016/j.ceramint.2019.05.187

47. A.K. Nikumbh, R.A. Pawar, D.V. Nighot, G.S. Gugale, M.D. Sangale, M.B. Khanvilkar, A.V. Nagawade, Structural, electrical, magnetic and dielectric properties of rare-earth substituted cobalt ferrites nanoparticles synthesized by the co-precipitation method. J. Magn. Magn. Mater. **355**, 201–209 (2014)
48. A.S. Nesaraj, S. Dheenadayalan, I. Arul Raj, R. Pattabiraman, Wet chemical synthesis and characterization of strontium-doped $LaLaFeO_3$ cathodes for an intermediate temperature solid oxide fuel cell application. J. Ceram. Process. Res. **13**, 601–606 (2012)
49. H.M. El-Mallah, AC electrical conductivity and dielectric properties of perovskite (Pb, Ca)TiO_3 ceramic. Acta Phys. Polon. A **122**, 174 (2012)
50. K.K. Patankar, P.D. Dombale, V.L. Mathe, S.A. Patil, R.N. Patil, AC conductivity and magnetoelectric effect in $MnFe_{1.8}Cr_{0.2}O_4$–$BaTiO_3$ composites. Mater. Sci. Eng. B **8**, 53 (2001)
51. M. Ajmal, N.A. Shah, A. Maqsood, M.S. Awan, M. Arif, Influence of sintering time on the structural, electrical and magnetic properties of polycrystalline $Cu_{0.6}Zn_{0.4}Fe_2O_4$ ferrites. J. Alloys Compd. **508**, 226–232 (2010)
52. G. Sathishkumar, C. Venkataraju, K. Sivakumar, Synthesis structural and dielectric studies of nickel substituted cobalt–zinc ferrite. Mater. Sci. Appl. **1**, 19–24 (2010)
53. M.R. Bhandare, H.V. Jamadar, A.T. Pathan, B.K. Chougule, A.M. Shaikh, Dielectric properties of Cu substituted $Ni_{0.5-x}Zn_{0.3}Mg_{0.2}Fe_2O_4$ ferrites. J. Alloys Compd. **509**, L113–L118 (2011)